AGU ADVANCING EARTH AND SPACE SCIENCE

Space Weather

RESEARCH ARTICLE
10.1029/2020SW002489

Key Points:

- A "perfect" ICME arrival at Earth is simulated using the Space Weather Modeling Framework
- Predicted surface dB/dt surpasses 30 nT/s above 45° latitude and 290 nT/s at local noon and 65° latitude
- Simulated response surpasses that of historically recorded extreme events, advancing our understanding of a space weather worst-case scenario

Supporting Information:

- Figure S1

Correspondence to:
D. T. Welling,
daniel.welling@uta.edu

Citation:
Welling, D. T., Love, J. J., Rigler, E. J., Oliveira, D. M., Komar, C. M., & Morley, S. K. (2021). Numerical simulations of the geospace response to the arrival of an idealized perfect interplanetary coronal mass ejection. *Space Weather*, *19*, e2020SW002489. https://doi.org/10.1029/2020SW002489

Received 26 FEB 2020
Accepted 30 NOV 2020

Numerical Simulations of the Geospace Response to the Arrival of an Idealized Perfect Interplanetary Coronal Mass Ejection

Daniel T. Welling[1], Jeffrey J. Love[2], E. Joshua Rigler[2], Denny M. Oliveira[3,4], Colin M. Komar[5,4], and Steven K. Morley[6]

[1]Department of Physics, University of Texas at Arlington, Arlington, TX, USA, [2]Geomagnetism Program, Geologic Hazards Science Center, U.S. Geological Survey, Denver, CO, USA, [3]Goddard Planetary Heliophysics Institute, University of Maryland, Baltimore, MD, USA, [4]Geospace Physics Laboratory, NASA Goddard Space Flight Center, Greenbelt, MD, USA, [5]Department of Physics, The Catholic University of America, Washington, DC, USA, [6]Space Science and Applications, Los Alamos National Laboratory, Los Alamos, NM, USA

Abstract Previously, Tsurutani and Lakhina (2014, https://doi.org/10.1002/2013GL058825) created estimates for a "perfect" interplanetary coronal mass ejection and performed simple calculations for the response of geospace, including dB / dt. In this study, these estimates are used to drive a coupled magnetohydrodynamic-ring current-ionosphere model of geospace to obtain more physically accurate estimates of the geospace response to such an event. The sudden impulse phase is examined and compared to the estimations of Tsurutani and Lakhina (2014, https://doi.org/10.1002/2013GL058825). The physics-based simulation yields similar estimates for Dst rise, magnetopause compression, and equatorial dB / dt values as the previous study. However, results diverge away from the equator. dB / dt values in excess of 30 nT/s are found as low as 40° magnetic latitude. Under southward interplanetary magnetic field conditions, magnetopause erosion combines with strong region one Birkeland currents to intensify the dB / dt response. Values obtained here surpass those found in historically recorded events and set the upper threshold of extreme geomagnetically induced current activity at Earth.

Plain Language Summary Space weather can induce strong currents through the power grid, damaging and disabling the network. Previous work produced idealized estimates of the worst-case-scenario space weather event and its impact on Earth. This study uses state-of-the-art computer models to further investigate the worst-case-scenario space weather storm and the effects on the Earth's surface. The rate of change of the magnetic field, a proxy for the induced current, is calculated. The previous work only considered the equatorial region; at mid and high latitudes, it is now found that the rate of change of the magnetic field can exceed the equatorial values by a factor of 10 or more. The latitude and longitude about the globe most strongly affected by such a storm is also investigated. This result exceeds values observed during historic extreme events, including the March 1989 event that brought down the Hydro-Québec power grid in eastern Canada.

1. Introduction

With the arrival at Earth of the shock wave of an Interplanetary Coronal Mass Ejection (ICME), a geomagnetic Sudden Impulse (SI) is generated in ground-level magnetometer data (e.g., Araki, 1977; Joselyn & Tsurutani, 1990), prominently seen in the horizontal component data acquired at low-latitude and midlatitude ground-based observatories. Magnetic storms often commence with such an impulse, and the most intense magnetic storms always commence with an impulse (e.g., Gonzalez et al., 2011). The future occurrence of rare magnetic super storms could have widespread deleterious impacts on modern technological systems (Cannon et al., 2013; National Research Committee on the Societal and Economic Impacts of Severe Space Weather Events, 2008). In this context, the Carrington event of 1859 has taken on particular significance—it is, by some estimates, the most intense magnetic storm ever directly measured (Lakhina et al., 2012; Tsurutani, 2003). Fundamental research into the physical nature of extreme space weather events has included data-driven, numerical simulation of a Carrington-class ICME (Manchester

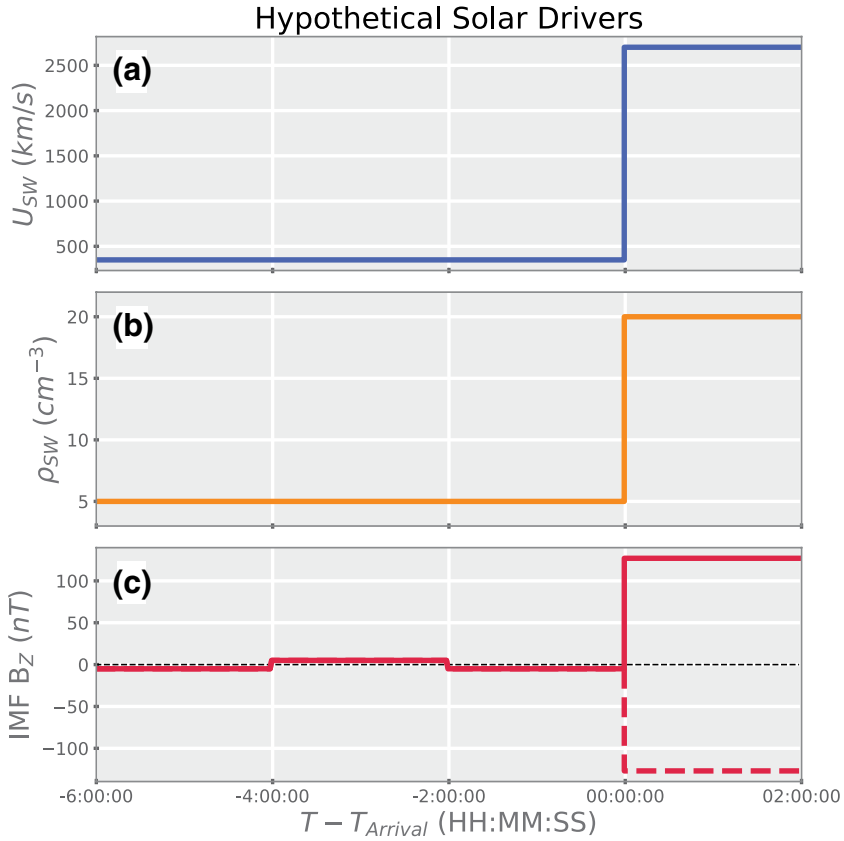

Figure 1. Solar wind and IMF drivers for the hypothetical extreme storm sudden commencement event. Top frame shows earthward solar wind velocity in units of km/s. The center frame shows solar wind number density in AMU/cm^3. The bottom frame shows the Z component (GSM system) of the IMF; solid line is the purely northward IMF case and the dashed line is the purely southward IMF case. Time is shown relative to the arrival time of the ICME at Earth. IMF, Interplanetary Magnetic Field; ICME, Interplanetary Coronal Mass Ejection.

et al., 2006), ICME-driven sudden commencement action on the magnetosphere-ionosphere system (Ridley et al., 2006), and simulation of the resulting storm main phase (e.g., Li et al., 2006; Ngwira et al., 2014).

Recently, Tsurutani and Lakhina (2014) have estimated, on the basis of qualitative physical arguments, solar wind parameters at 1 astronomical unit for a theoretically most-extreme ICME. They refer to these as the conditions of a "perfect" ICME. They infer that these conditions would generate a giant sudden impulse and a magnetic storm having an intensity far exceeding anything ever measured. They suggest, furthermore, that the hazards of such a hypothetical event, especially hazards to electric-power grids posed by the induction of geoelectric fields in the conducting solid Earth and the resulting Geomagnetically Induced Currents (GICs), should be further studied. Motivated by the work of Tsurutani and Lakhina (2014), we use their estimates of the "perfect" ICME to drive a numerical simulation of the response of the coupled ionosphere-magnetosphere system to the sudden impulse during the ICME's arrival. Results inform projects concerned with the assessment and mitigation of space weather related hazards and risks (Eastwood et al., 2017), such as the National Science and Technology Council (2015) and allied international organizations (e.g., Schrijver, 2015).

2. Solar Wind Conditions

The solar wind conditions preceding and during the hypothetical "perfect" sudden commencement event are adapted from Tsurutani and Lakhina (2014) and are illustrated in Figure 1. Values are plotted against time relative to the epoch of the ICME arrival at the bow shock with negative values indicating time before arrival. For the first 6 h, an ambient solar wind velocity of 350 km/s and density of 5 AMU/cm^3 are used.

The Interplanetary Magnetic Field (IMF) during this period is oriented purely southward with a magnitude of −5 nT. Four hours before arrival, the IMF turns northward for a period of 2 h before returning southward. This sets up more realistic magnetospheric conditions in the numerical simulation. Conditions then impulsively change following the analysis of Tsurutani and Lakhina (2014). The velocity jumps to 2,700 km/s. This assumes a near-Sun ICME speed of 3,000 km/s that is only slowed 10% by an inner heliosphere that has been recently "cleaned out" by a recent preceding ICME. The ICME density jumps to 20 AMU/cm^3 using a shock jump ratio of 4. The IMF magnitude changes to 127 nT based on the empirical relationship from Gonzalez et al. (1998). Two separate orientations for the IMF jump are considered here: a northward IMF case and a southward IMF case. A purely frontal shock is assumed as these shocks can result in stronger geomagnetic activity (Oliveira et al., 2018; Oliveira & Raeder, 2014, 2015), even though shocks with small impact angles are correlated with faster sudden impulse rise times (e.g., Guo et al., 2005; Wang et al., 2006). The result of these assumptions and those made by Tsurutani and Lakhina (2014) is input conditions for a hypothetically "perfect" single sudden commencement event. Time series data are available in the repository listed in the acknowledgments.

3. Modeling Method

The interaction of these solar wind drivers with the Earth's magnetosphere and ionosphere are simulated using the Space Weather Modeling Framework (SWMF) (Tóth et al., 2005, 2012). The SWMF executes, synchronizes, and couples different models of the space environment to obtain a complete description of magnetosphere-ionosphere dynamics. For this simulation, three models are employed. The first is the Block Adaptive Tree Solar wind Roe-type Upwind Scheme (BATS-R-US) code, a flexible, finite-volume Magnetohydrodynamic (MHD) model (Powell et al., 1999; De Zeeuw et al., 2000; Groth et al., 2000). BATS-R-US has a long history of terrestrial magnetosphere simulations (e.g., Song et al., 1999; Zhang et al., 2007; Ilie et al., 2010; Welling & Zaharia, 2012) including simulations of extreme driving (Ridley et al., 2006; Ngwira et al., 2013, 2014). BATS-R-US MHD uses an eight-wave formulation of the MHD equations Powell et al. (1999), which maintains $\nabla \cdot \vec{B} = 0$ to truncation error and does not require additional $\nabla \cdot \vec{B}$ (Tóth, 2000). Via the SWMF, it is coupled to a height-integrated ionospheric electrodynamics model (Ridley et al., 2001), which calculates the ionospheric electric potential and horizontal currents from the MHD Birkeland currents. The electric potential is returned to BATS-R-US to set the convection electric field. Conductance from both solar Extreme Ultraviolet Radiation (EUV) and the aurora are included. The former is achieved via an empirical function of solar zenith angle and F10.7 solar radio flux (Moen & Brekke, 1993). The latter is set by an empirical function of the local Birkeland current strength (Mukhopadhyay et al., 2020; Ridley et al., 2001). To better capture ring current dynamics, the Rice Convection Model (RCM) (Harel et al., 1981; Sazykin & Stanislav, 2000; Toffoletto et al., 2003) is also employed. It receives plasma sheet conditions, magnetic and electric fields from the other models and returns plasma pressure and number density to BATS-R-US (De Zeeuw et al., 2004). Because the ring current has little time to develop after storm arrival, the predominant role of RCM in this study is to help develop a more realistic prestorm magnetosphere.

Overall, this configuration of the SWMF is an appropriate and capable model for this simulation, but shortcomings must be considered. The SWMF has been validated in terms of magnetospheric dynamics (Rastätter et al., 2011; Ridley et al., 2002; Welling & Ridley, 2010; Welling et al., 2015), Birkeland current distributions (Korth et al., 2011), ground magnetic perturbations (Yu & Ridley, 2008, 2009b), and associated geomagnetic indices (Glocer, 2016; Haiducek et al., 2017; Rastätter et al., 2013). The finer spatial grid resolution used in this study greatly improves data-model comparisons in terms of auroral electrojet index performance (Haiducek et al., 2017), Birkeland current morphology (e.g., Welling et al., 2015), and integrated Birkeland current strength (Mukhopadhyay et al., 2020), overcoming some of the limitations explored in Anderson et al. (2017). The SWMF has demonstrated skill in forecasting surface dB / dt using its operational configuration (Pulkkinen et al., 2013) as quantified by the Heidke Skill Score (HSS), a value that presents the fraction of correct binary forecasts (in this case, events where dB / dt crosses a given threshold within a given time window) after accounting for correct forecasts obtainable by random guess (Jolliffe & Stephenson, 2012). Reported Heidke Skill Scores diminish at higher dB / dt thresholds, however. Specifically, Welling et al. (2017) demonstrated that for stronger solar driving, the model is most likely to under predict dB / dt. Again, the situation is improved for the finer grid resolution employed in this study.

For example, the Heidke Skill Score for dB / dt at the 1.5 nT/s threshold improves from 0.318 (i.e., the model captures 31.8% of threshold crossings not captured by random guessing) to 0.4094 (Mukhopadhyay et al., 2020). It is critical to recognize that these scores encompass all activity, including periods when the model struggles, such as substorms (e.g., Haiducek et al., 2020). Figures 3 and 4 of Pulkkinen et al. (2013) demonstrate that MHD models tend to perform more strongly at the beginning of storms, but this effect has yet to be quantified. As such, the dB / dt estimates should be considered lower limits for real-world values. Welling (2019) presents in-depth review of the state of MHD modeling of surface magnetic perturbations, including validation, strengths, and limitations.

The exact configuration of these models follows Pulkkinen et al. (2013) with some notable exceptions:

1. The inner boundary is set at 1.75 R_E instead of 2.5 R_E. This prevents situations where the magnetopause touches the inner boundary under extreme driving
2. The grid resolution follows Figure 1 of Welling and Ridley (2010). Near the inner boundary, cell sizes are cubes of 1 / 8 R_E width. The inner magnetosphere and magnetopause during the SI lie within regions of 1 / 4 R_E cell size
3. All models are coupled at a frequency of 1 Hz, as opposed to typical values of 0.1 Hz. This ensures the models stay synchronized during the rapid SI
4. To simplify analysis, the dipole tilt is set to zero, i.e., the magnetic dipole is aligned with the rotation axis

Input files are available in the repository listed in the acknowledgments. Using this setup, two simulations are performed: a purely northward IMF sudden commencement and a purely southward IMF case.

Ground magnetic perturbations are calculated using chains of *virtual magnetometers* (Yu & Ridley, 2009b). These are probes of the coupled-model system that perform Biot-Savart integrals of four distinct current systems:

1. All currents within the MHD domain
2. Birkeland currents in the "gap region" between the MHD inner boundary and the ionosphere, mapped along assumed dipole field lines
3. Ionospheric Hall currents
4. Ionospheric Pedersen currents

The four contributions are used to calculate the total perturbation in three orthogonal directions; only the two horizontal components (north-south, "X" and east-west, "Y") are examined here. Because the geomagnetic axis is set to be parallel with the Earth's rotational axis in this simulation, geomagnetic and geographic directions are equivalent. Virtual magnetometer results have 1 Hz resolution. The efficacy of these tools in reproducing observations and their role in space weather forecasting has recently been reviewed by Welling (2019). Virtual magnetometers show only the external magnetic field and do not capture the perturbations arising from inductive effects of the Earth itself.

4. Simulation Results

Figure 2 shows the response of the magnetosphere-ionosphere system to the hypothetical ICME arrival, for both the northward and southward cases. The top row of Figure 2 (frames a–d) illustrates the moment when the ICME shock wave arrives at the bow shock (approximately 6 h, 40 s after the start of the simulation, herein referred to as $T_{Arrival}$). At this point, the northward IMF case (frames a and b) is the same as the southward case (frames c and d). Forty seconds later (second row, frames e–i), the ICME has begun to compress the magnetosphere. In agreement with previous studies of sudden impulses in global MHD models (Kataoka et al., 2004; Slinker et al., 1999; Yu & Ridley, 2009a), low-latitude flow vortices form along the day side magnetopause and propagate with the shock to the night side (not shown). These drive Birkeland currents connecting to the day side ionosphere (frames f and g), propagating to the night side with the associated magnetospheric flow vortices. At $T_{Arrival}$ + 1 : 10 (Figure 2, third row), the two cases begin to diverge. The southward oriented IMF begins to erode the day side magnetopause rapidly (frame l), driving the magnetopause farther inwards compared to the northward IMF case (frame i). While the spatial distribution of the Birkeland currents are similar between the two cases, the additional contribution from reconnection-driven Birkeland currents creates stronger currents in the southward IMF case (3.3 μ/Am^2 peak, frame (k) as

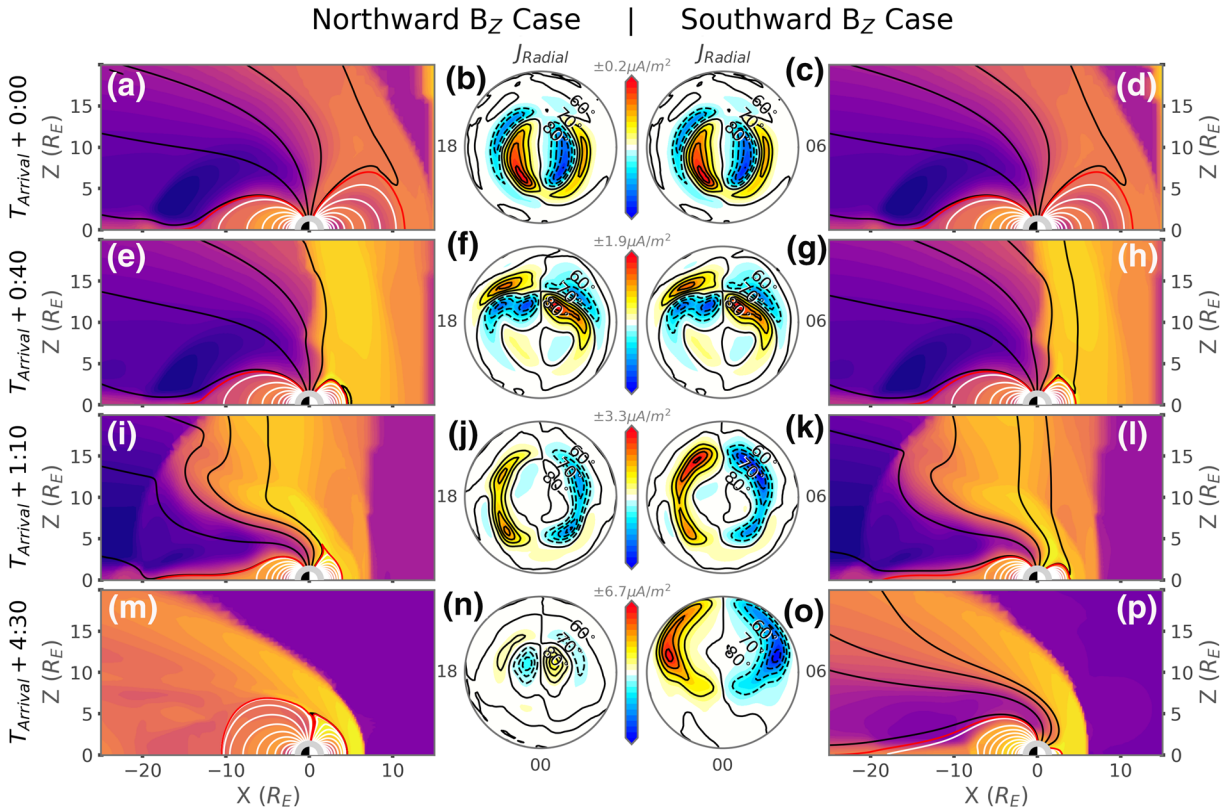

Figure 2. Simulation results for the ICME arrival at the magnetosphere. Each row shows results from a different point in the simulation. Results for the northward IMF case are shown in the leftmost two columns, results for the southward case on the right. The leftmost and rightmost columns show the state of the magnetosphere in the noon-midnight meridian plane in terms of magnetic field (black lines for open field, white lines for closed field, and red lines for the last-closed line) and plasma thermal pressure (colored contours, shown without scale for the purposes of characterizing magnetospheric geometry only). The polar plots illustrate the Birkeland currents flowing into (blue) and out of (yellow) the northern hemisphere. The scale of the current contours is shown via the color bar at the center of the figure. A version of this figure that shows the scale of the pressure can be found in the supporting information (Figure S1). IMF, Interplanetary Magnetic Field; ICME, Interplanetary Coronal Mass Ejection.

compared to the northward case (frame j). After passage of the ICME ($T_{Arrival}$ + 4 : 30, bottom row), the two simulations have relaxed into a new pseudosteady state. Dynamics are well characterized by forward and reverse magnetospheric convection; typical Birkeland current patterns for the southward and northward case, respectively. Again, reconnection has eroded the magnetopause farther inward in the southward case (frame p) than in the northward case (frame m), where compression acts alone. Noteworthy for the southward case (frame o) is the extreme Birkeland current amplitudes (6.7 μ/Am^2) and their low latitudes on the day side due to magnetopause erosion.

The simulated D_{ST} values illustrate the impact of the ICME arrival. Figure 3a shows high time resolution D_{ST}-equivalent from the northward IMF and southward IMF cases. Values are plotted against time relative to $T_{Arrival}$. The fast, sudden rise of D_{ST} indicates the development of magnetopause currents; the difference of D_{ST} from precompression to peak is one measure of the strength of the storm sudden impulse. For the northward case, D_{ST} reaches a peak of 234.0 nT, slightly lower than the Tsurutani and Lakhina (2014) estimate of 245 nT. For the southward case, the peak D_{ST} is of larger magnitude (268.7 nT) and is reached slightly sooner than the northward IMF case. Despite small differences between the northward and southward cases, both are congruent with the estimates of Tsurutani and Lakhina (2014).

Before the simulated ICME makes contact with the bow shock ($T < T_{Arrival}$), a precursor signature is observed in D_{ST}. These signatures arise from the intense current sheet that forms at the IMF discontinuity as it jumps from −5 nT to ±127 nT. Because the virtual D_{ST} is the result of a Biot-Savart integral covering the entire MHD domain, the ICME current sheet begins to drive prearrival signatures as soon as it enters the MHD model's upstream boundary at +32 R_E. Immediately before impulse onset, the precursor signature

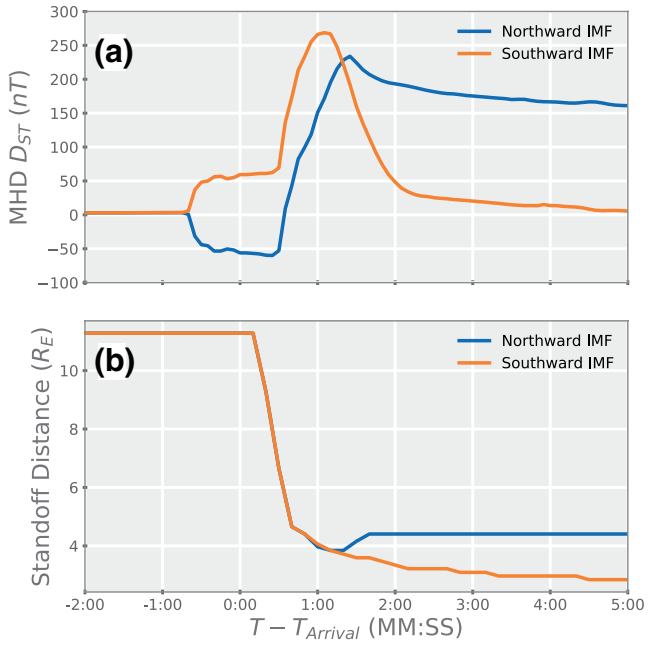

Figure 3. Summary of the northward IMF (blue) and southward IMF (orange) simulated sudden impulse in terms of the D_{ST} index (frame a) and the magnetopause stand-off distance (frame b). IMF, Interplanetary Magnetic Field.

reaches ±50 nT (Figure 3a), growing slightly as the shock approaches Earth, with the orientation corresponding to the direction of the IMF. The addition of the precursor signal to the sudden impulse signal can explain the differences in magnitude and timing between the northward and southward IMF cases. This signal is a result of the magnetostatic assumption implicit in the Biot-Savart integral. Under the more realistic MHD formalism, such a magnetic signal propagates with local plasma wave speeds and could not arrive faster than the shock, as the relevant upstream Mach numbers are all greater than 1.

Figure 3b shows the magnetopause stand-off distance for both the northward and southward IMF cases. The values are calculated by identifying the first computational cell in the MHD domain whose field line is open to the solar wind when progressing radially from the Sun to the Earth. Initial compression precedes the formation of significant magnetopause currents (as detected by the D_{ST} signal in Figure 3a) by approximately 20 s as, initially, the Earth's field rapidly retreats from the incoming ICME. The ICME leads to extreme compression of the day side magnetosphere. Though the magnetopause is pushed very close to the inner boundary, several grid cells separate the two. For the northward IMF case, the stand-off distance reaches a new equilibrium at 4.41 R_E, reasonably agreeing with the estimate from Tsurutani and Lakhina (2014) of ~ 5 R_E. For the southward case, day side reconnection further erodes the magnetopause to a stand-off distance of 2.84 R_E. The polarity of the IMF is clearly an important factor in setting the stand-off distance.

Figure 4 shows the effect of the ICME on the surface magnetic field in the geomagnetic north-south direction for a latitudinal chain of virtual magnetometers all located at local noon (12LT). The figure covers 7 min of the event. Both the magnetic perturbation (ΔB_N, frames a and c) as well as the time derivative (dB_N / dt, frames b and d) are shown. The geomagnetic east-west component results (not shown) are drastically weaker than the north-south component, except at auroral latitudes where the values are of the same order as the north-south component.

Starting with the northward IMF case (Figure 4, frames a and b), it can be seen that the impulse onset organizes itself into three distinct phases. The first phase is the precursor phase, where the current sheet within the IMF discontinuity is driving the precursor signal at all latitudes and local times. The strength of the disturbance grows to −50 nT at middle latitudes. The second phase, beginning at ~30 s after ICME arrival and lasting until ~120 s after arrival, is the sudden impulse phase. The ground magnetometers exhibit dynamics closely following well-established patterns from observations (Araki, 1977; Araki et al., 1997) and previous MHD simulations (Kataoka et al., 2004; Slinker et al., 1999; Yu & Ridley, 2009b) at all local times. The ΔB_N magnitude reaches 300 nT at midlatitudes and more than 900 nT at auroral latitudes. For the northward IMF case, this is the period of the most intense dB_N / dt values (frame b). At low-latitudes and midlatitudes, values agree with the estimates from Tsurutani and Lakhina (2014) (~30 nT/s). At higher latitudes, extreme dB_N / dt values are observed (>200 nT/s). The final phase of the event is the formation of perturbations related to the establishment of Dungey-cycle magnetospheric convection as the system reaches a new steady state configuration. Region-1 Birkeland currents form, driving perturbations on the order of several hundred nanotesla. These become static as the system settles, reducing dB_N / dt values to zero.

Frames c and d of Figure 4 illustrate the same as frames a and b, but for the case where IMF is southward. Note that the scale of the ΔB_N plot has changed (frame c); the distance between two zero lines (dashed lines) is now 800 nT instead of 300 nT (as in frame a). Again, three phases are evident: the precursor, the sudden impulse signature, and perturbations related to the development of typical region-1 Birkeland currents. Because the polarity of the IMF has changed, the polarity of the precursor signature has flipped. Because the ICME shock is identical to the northward case in terms of dynamic pressure, the sudden impulse signatures are identical, both in terms of polarity, magnitude, and dB / dt. Through the first two phases, the polarity of the IMF plays only a minor role.

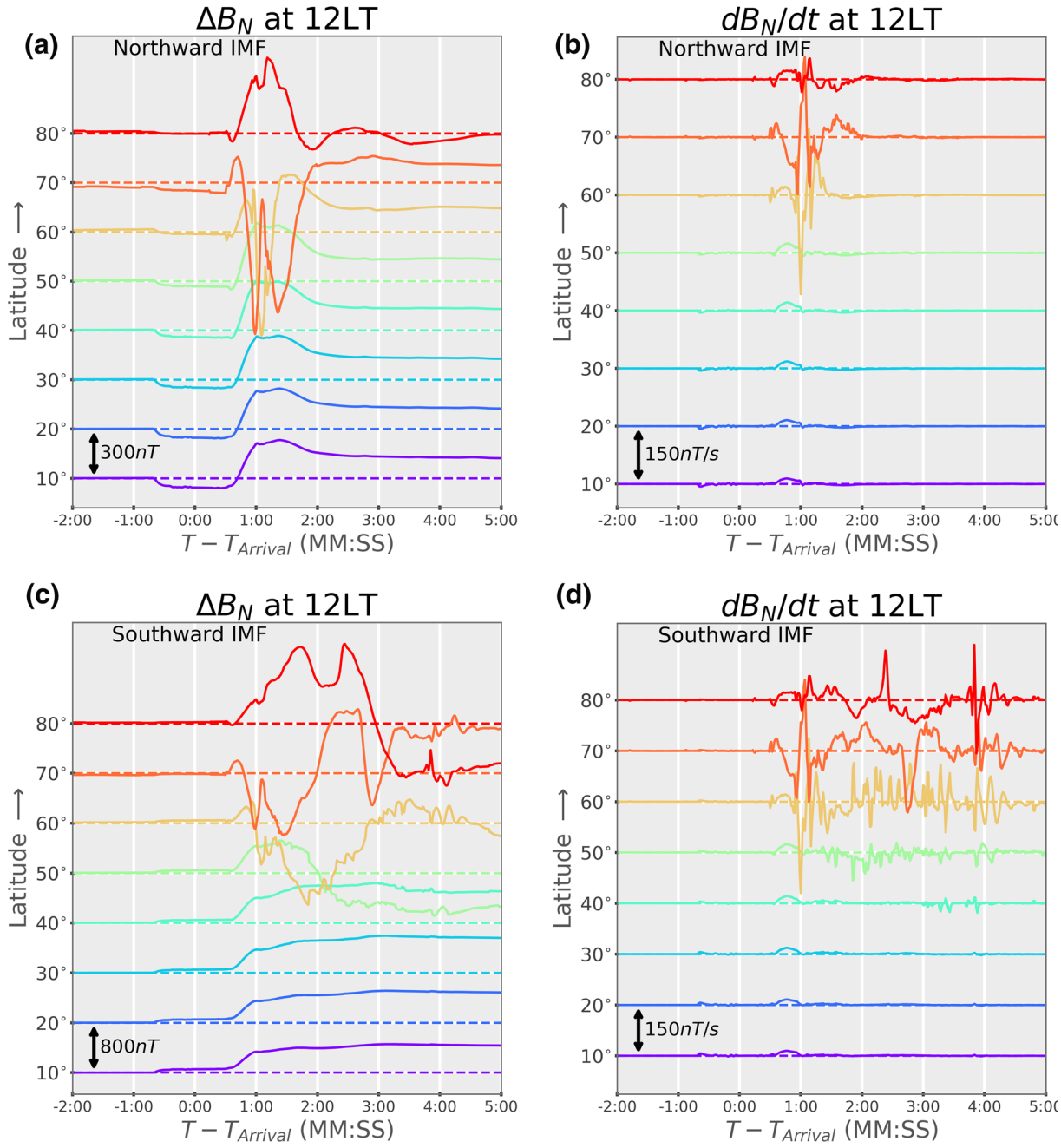

Figure 4. Virtual magnetometer surface perturbation results in the magnetic north-south direction for stations situated at local noon, 2 min before shock arrival through 5 min afterward. Both ΔB_N (left column) and dB_N / dt (right column) are shown. Top row (frames a and b) shows results for the northward IMF case; bottom row (frames c and d) shows the results for the southward case. Stations are arranged in latitudinal order with the lowest latitudes on the bottom. For each curve, the dashed line of the same color shows where $\Delta B_N = 0$ or $dB_N / dt = 0$. The black arrow in the lower left of each frame shows the scale of the perturbations. IMF, Interplanetary Magnetic Field.

The final phase of the commencement stands in stark contrast to the northward IMF case. The southward oriented IMF drives intense reconnection and associated region-1 Birkeland currents. These develop quickly and concurrently with the end of the sudden commencement signature. The superposition of the sudden commencement signal and the intense Birkeland current signal creates ΔB perturbations that reach into the thousands of nanotesla with dB / dt values that reach 290 nT/s. The final phase of the event prolongs the GIC threat beyond what is presented by the northward case. The erosion of the day side magnetopause also

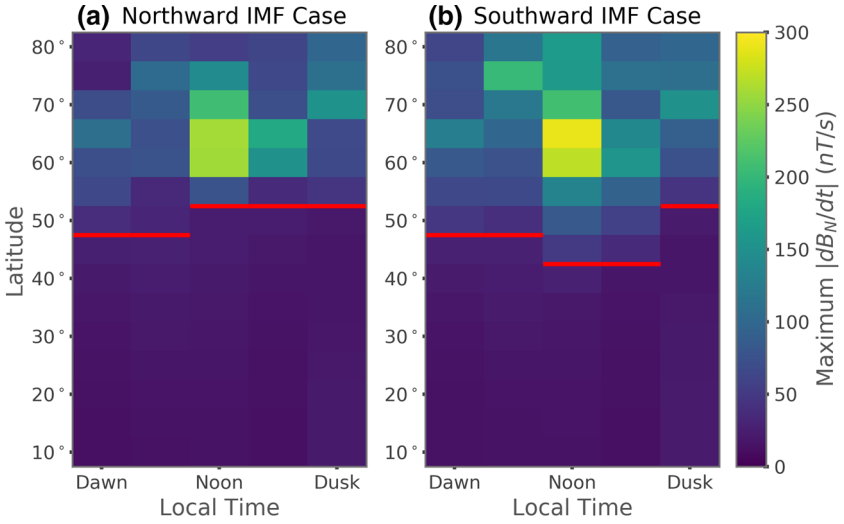

Figure 5. Maximum dB_N / dt from −2:00 < T-$T_{Arrival}$ < 5:00 as a function of local time (x-axis) and latitude (y-axis). Results for the northward and southward case (frames a and b, respectively) are shown. Red lines mark the contour of 30 nT/s.

brings the Birkeland currents to lower latitudes on the day side, bringing the threat over more populated areas of the globe.

The magnitudes of dB / dt are dependent both on latitude and longitude. Figure 5 summarizes the maximum dB_N / dt for −2:00 < T-$T_{Arrival}$ < 5:00 and local times between dawn and dusk. On the night side, convoluted tail dynamics present a complicated picture that require further evaluation and will not be addressed here. East-west component values remain at or below the north-south values shown in Figure 5. The red lines in Figure 5 mark the latitude boundary above which dB / dt > 30 nT/s, i.e., surpassing the dB / dt estimates of Tsurutani and Lakhina (2014).

Figure 5 illustrates the danger presented during the arrival of a "perfect," isolated ICME. It is evident that the strongest dB / dt values occur at local noon between 55° and 65° latitude. However, extreme values appear across a large region of the figure: latitudinal boundaries form such that northward of these boundaries, dB / dt exceeds 30 nT/s at all day side local times (red lines in Figure 5). For the northward IMF case (frame a), this boundary straddles 50°. For the southward IMF case (frame b), this boundary reaches as low as 40°. It is important to note that because these simulations used a simplified dipole axis, extreme dB / dt could reach lower geographic latitudes in a real-world situation, easily encroaching into the continental United States of America.

Finally, the ground magnetic disturbance produced by the model is used to calculate geoelectric field. Finally, ground-level geomagnetic disturbance, together with an estimated surface impedance, can be used to calculate a geoelectric field (Pirjola, 2002; Love, Bedrosian, et al., 2019). The plane-wave method is used to obtain these values (Pirjola, 1985; Simpson & Taflove, 2005; Wait, 1982). Because geoelectric field is highly sensitive to ground conductivity, and because these values are poorly constrained in most places, several simplified situations are presented here. First, two uniform half-space ground conductivity models are employed: a resistive case representative of dry igneous and metamorphic rock (10,000 Ω/m) and a conductive case representative of wet sedimentary rock (1 Ω/m) (Palacky, 1988). These profiles are applied at a range of latitudes. To further explore possible ground responses, the ground conductance profile of Québec, Canada, is used in conjunction with model results at 55° magnetic latitude. This profile is quite resistive, yielding a strong, but not necessarily worst-case values. It allows for direct comparison to the March 1989 "Hydro-Québec" historic extreme and to other simulations of hypothetical extreme events. Two ground conductivity profiles were used to represent this region: the five-layer Québec model and the six-layer Québec model (see Boteler (2015), models 3 and 4, respectively). The Québec models represent a resistive case; Woodroffe et al. (2016) found the six-layer model is, on average, around the 80th percentile

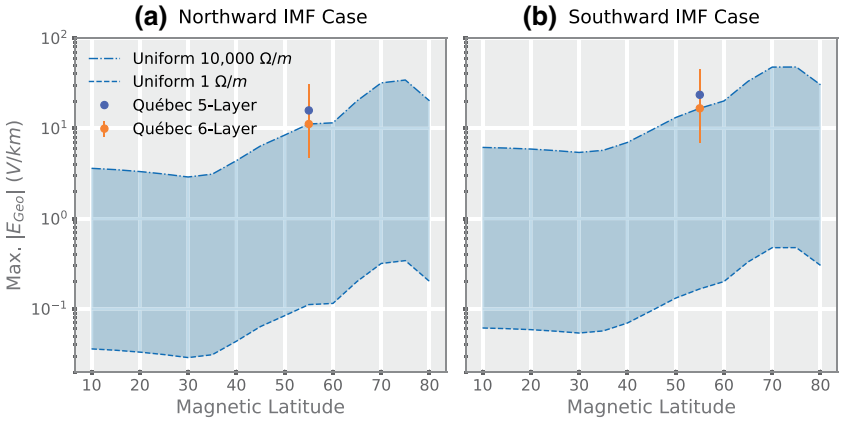

Figure 6. Maximum geoeletric field amplitude as a function of latitude for the northward (left frame) and southward (right frame) IMF case. Line color indicates ground conductivity model used to obtain field values. Light blue region indicates uncertainty in values from the six-layer conductivity model. IMF, Interplanetary Magnetic Field.

in magnitude of response. To illustrate the effect of the uncertainty in this calculation, geoelectric field was recalculated using the six-layer model using a factor of three and a factor of 1/3. This follows the procedure used by Boteler (2015). It must be emphasized that the following results for geoelectric field represent only an initial study of this value; a more in-depth exploration that uses 3D conductivities is required in future studies. Nevertheless, these simple values help place the impact of this event into context among its peers.

Figure 6 illustrates the maximum horizontal magnitude of the geoelectric field as a function of latitude. The maximum is taken as the largest value after the ICME arrival at a given latitude at local noon. Results obtained using the resistive and conductive half-space models are shown as the dashed and dotted blue lines; the range of values these cases span are shaded blue. At 55° magnetic latitude, geoelectric field values using the five-layer and six-layer Québec model conductivity models are shown as blue and orange dots, respectively; the range of uncertainty in the six-layer-based results are shown via orange error bar. Foremost, this figure illustrates the large range of potential field values possible given different ground conditions. Geoelectric fields are highly dependent on ground conductivity profiles; much uncertainty remains with these values. This figure also shows that the geoelectric field from such an ICME arrival would be massive in regions where the Earth is resistive. For the northward case, shown in Figure 6a, the maximum electric field (assuming a resistive ground conductivity profile) surpasses 10 V/km at a geomagnetic latitude as low as 53° and peaks at higher latitudes between ~34.4 V/km. Conditions intensify for the southward case, shown in Figure 6b. Values reach 10 V/km near 45° geomagnetic latitude and peak at ~47.7 V/km for resistive ground conditions.

5. Historical Context

Table 1 places the results of the above simulations in the context of other simulations and real-world observations of extreme sudden commencements. Where available, the impulse as measured by Dst (or equivalent), the magnetopause stand-off distance, maximum reported dB / dt, and estimated geoelectric field are listed. For the simulations presented in this study, both overall maximum dB / dt and equatorial values (denoted by 0° in Table 1) are given. Note that dB / dt is sensitive to the sampling frequency of ΔB, and this is not controlled for here. For geoelectric field from the simulations performed in this study (second and third rows of results), maximums are first given over all latitudes using both conductive and resistive ground conductivity cases. Values are also reported at 55° magnetic latitude (corresponding to the latitude of Québec, Canada) using the five- and six-layer Québec conductivity models. Geoelectric field values from other studies shown in Table 1 were calculated using either the five-layer or six-layer Québec conductivity models at all latitudes. The five-layer model in particular is very resistive and will yield extreme results, especially as it is not applicable away from Québec. All estimates of geoelectric field in Table 1 were obtained using the plane-wave method as used here. Northward and southward IMF cases are indicated by NB_Z and

Table 1
Comparison of Simulation Results to Other Extreme Space Weather Events & Simulations

Event/simulation	D_{ST} Impulse	Standoff	Max *dB/dt*	Max |*E*
T & L Estimates[a]	245 nT	5 R_E	30 nT/s	N/A
Present results: NB_Z	234.0 nT	4 R_E	260 nT/s	0.34–34.3 V/km
			12 nT/s at 0°	11.2–15.8 V/km at 55°
Present results: SB_Z	268.7 nT	< 3R_E	290 nT/s	0.48–47.7 V/km
			12 nT/s at 0°	16.7–23.5 V/km at 55°
Synthetic Carrington[b]	< 200 nT	> 2 R_E	N/A	> 30 V/km
				> 17 V/km at 55°
July 2012 near-miss[c,d]	N/A	N/A	~ 10 nT/s	~ 15 V/km
				~ 15 V/km at 55°
September 1909 Storm[e]	~ 70.0 nT	5.9 R_E	N/A	N/A
May 1921 Storm[f]	~ 107.0 nT	5.3 R_E	N/A	N/A
March 1989 Storm[g,h,i]	~ 70 nT	N/A	~ 20 nT/s	> 3 V/km at 55°
March 1991 Storm[j,k]	202 nT	N/A	~ 20 nT/s at MSR	N/A

Values for the March 24, 1991 event are taken from the Moshiri magnetometer Station (MSR) at 37.9° magnetic latitude. [a]Tsurutani and Lakhina (2014). [b]Ngwira et al. (2014). [c]Baker et al. (2013). [d]Ngwira et al. (2013). [e]Love, Hayakawa, and Cliver (2019b). [f]Love, Hayakawa, and Cliver (2019a). [g]Kappenman (2005). [h]Boteler (2019). [i]Allen et al. (1989). [j]Araki et al. (1997). [k]Araki (2014).

SB_Z, respectively. While not an exhaustive list, it emphasizes the most prominent space weather events that should be comparable to the hypothetical ICME in question.

The hypothetical most-extreme storm sudden commencement simulated here surpasses magnitudes presented by historic extremes. Estimates from the Tsurutani and Lakhina (2014) study (Table 1, top row) are accurate in terms of the strength of the impulse as measured by D_{ST}, but underestimate compression/erosion of the day side magnetopause and did not report the more intense *dB* / *dt* values at midlatitudes to high latitudes. An attempt to produce conditions similar to the famous Carrington Event (fourth row) yields magnetopause compression similar to that found here, but a weaker sudden commencement D_{ST}. "What If" simulations of the July 2012 near-miss extreme ICME (Ngwira et al., 2013; fifth row) show that it would not have produced a significant sudden commencement; peak *dB* / *dt* for this hypothetical were much lower than those found in this study. For both of these synthetic events, the geoelectric field values near 55° geomagnetic latitude were calculated using the five-layer Québec conductivity model, corresponding to the highest values produced by the simulation results here (15.8 and 23.5 V/km for the northward and southward IMF cases, respectively). The geomagnetic values from these other extreme simulations are similar to the northward IMF event of this study but surpassed by the southward IMF event. Neither reaches the overall maximum field values of either the northward or southward IMF configurations of the ICME simulated here. The September 1909 May 1921 "railroad," and the March 1989 "Hydro-Québec" historic extreme storms (Table 1, Rows 6–8, respectively) all delivered sudden commencements far weaker than the hypothetical worst-case explored here. The Hydro-Québec event of 1989 famously disrupted power distribution in eastern Canada; peak *dB* / *dt* values are as much as an order of magnitude less than those found in the present simulations. Estimates of geoelectric field during this event using ground magnetic observations from the Ottawa magnetic observatory and the same ground conductivity models as used here reports values just surpassing 3 V/km Boteler (2019); the values obtained via simulation for the ICME of this study surpasses this by a factor of 5. In each of the above cases, the characteristic magnitudes of the simulated worst-case scenario are notably greater.

One historic event stands out as being similar in magnitude to the hypothetical extreme explored here: the March 24, 1991 storm (Table 1, bottom row). This event produced an anomalously large sudden commencement as measured on the ground: 202 nT in the H-component of the Kakioka ground station (Araki

et al., 1997). While the overall storm is not as famous or destructive as the March 1989 event, large geomagnetically induced currents were reported in the Hydro-Québec (Bolduc, 2002) and northern European (Pirjola, 2005) power grids. A handful of other extreme storm sudden commencements with ground amplitudes commensurate with the present hypothetical worst-case simulations have been reported by Araki (2014), suggesting that the results here are not out of the realm of possibility.

Further context can be obtained by comparing the geoelectric field estimates calculated from the extreme storm sudden commencement simulation to estimates of 100 years geoelectric field values. From an analysis of magnetotelluric tensors and historical magnetic observatory data, Love, Lucas, et al. (2019) estimated 100 years geoelectric fields for sites across the Northeast United States, including as high as 25.44 V/km at one site in Virginia (geographic: 37.38°N, 77.58°W; geomagnetic: 46.57°N, 5.68°W) and as low as 0.05°V/km at another site (geographic: 37.88°N, 79.81°W; geomagnetic: 47.02°N, 8.28°W) also in Virginia. The wide range of values they find, at similar latitudes, is due to significant localized differences in surface impedance, such as roughly represented by our two half-space models. Figure 6 shows that the geoelectric fields from the extreme storm sudden impulse simulations to be of comparable order to those from (Love, Lucas, et al., 2019), but caution must be exercised in this comparison as Love, Lucas, et al. (2019) used full impedance tensors estimated from magnetotelluric observations. Using the plane-wave method and a conductive (British Columbia, Canada) and resistive (Québec, Canada) 1D ground models, Pulkkinen et al. (2012) also estimated 100 years values. Specifically, the resistive model is the same five-layer Québec model employed, in part, here (Figure 6, blue dots). They found 100 years amplitudes of 5–20 V/km depending on which conductance model was employed. This approach more closely resembles that used here. The geoelectric field values calculated from the extreme storm sudden commencement simulation results surpass the Pulkkinen et al. (2012) maximum of 20 V/km at a latitude of 65° and 60° for the northward and southward IMF case, respectively. Again, caution is emphasized as the true response is highly sensitive to local ground conditions.

6. Discussion and Conclusions

The low-latitude estimates of the impacts of a "perfect" ICME arrival at Earth, as defined by Tsurutani and Lakhina (2014), paint an incomplete picture of the full hazards of such an event. The first-principles-based simulations presented in this study show the full impact at a range of locations. Magnetopause compression exceeds the pressure-balance-based estimates from the previous work. The magnitude and nature of the ground magnetic perturbation are heavily location dependent. This analysis shows that the 30 nT/s estimates from Tsurutani and Lakhina (2014) are easily surpassed above ~ 45° geomagnetic latitude. Accounting for the dipole tilt and time of arrival means that densely populated lower geographic latitudes can be impacted by the extreme dB / dt values found in these simulations. While the day side is most strongly affected, extreme perturbations are generated across the globe. Though only the initial moments of such a "perfect" ICME event are considered, this sudden impulse would surpass historically recorded events in terms of dB / dt.

The orientation of the IMF plays a critical role in determining the severity of the ground magnetic perturbations during the impulse. As day side reconnection develops, erosion of the day side field combines with compression to drive the magnetopause within 3 R_E of the Earth. While compression-related magnetic perturbations between the purely northward and purely southward simulation are nearly identical, the development of intense region-1 Birkeland currents in the southward IMF case increase both the magnitude and the duration of the ground perturbations. The erosion of the day side magnetopause pushes these currents and their associated perturbations to far lower latitudes than the northward case. This means that even during the first moments of an extreme space weather storm, IMF orientation plays a critical role in determining the danger to vulnerable technological systems. Further exploring the parameter space of the IMF orientation will help quantify the full range of impacts as a function of impact angle (e.g., Oliveira & Raeder, 2014, 2015; Oliveira et al., 2018).

Many limitations must be considered when interpreting these results, starting with the construction of the idealized solar wind and IMF conditions. The work of Tsurutani and Lakhina (2014) merely provided amplitudes for solar wind dynamic pressure and IMF B_Z. Here, these amplitudes have been adapted into a

simple step function; the solar wind dynamic pressure and IMF impulsively reach extreme values in unison. In reality, a more complicated sheath region would form ahead of the cloud field, with strong oscillations in IMF and plasma conditions. The arrival of the extreme pressure pulse and the extreme ejecta field would then be separated by the sheath. In this situation, the sudden impulse phase of the dB / dt response would be separated in time from the response related to the formation of the Birkeland currents. While the magnitude of the response is not likely to change, the location of the peak disturbance could be affected if the solar wind dynamic pressure relaxes by the time of the extreme IMF arrival, affecting the latitude of current flow. A simultaneous jump in dynamic pressure and IMF from background to extreme values is only possible under a rare set of circumstances. One situation would be that the leading edge of the interplanetary shock catches up to the magnetic cloud of the previous event (recall that a previous event is assumed by Tsurutani and Lakhina (2014), clearing the slow solar wind ahead). The sheath field would then be the field from the preceding ICME, shocking it to higher values. While the surface field response would be similar, additional preconditioning effects would need to be considered, such as energization of the ring current and higher ionospheric conductances. Alternatively, the conditions could possibly arise from a complex sheath resulting from multiple eruptions, more closely resembling the idealized conditions simulated here. Aside from IMF, the plasma density used here, 20 AMU/cm^3, is frequently surpassed in real-world ICMEs. This could be considered a lower bound for a real-world event, though the assumption that a previous ICME clears out dense, ambient solar wind flow means that a high background density is not likely. While considering these factors should be a priority in the future, the results of this study still provide meaningful estimates of an extreme impulse.

Other model limitations and simplifications must also be considered. As discussed above, MHD models tend toward under prediction of dB / dt when compared to observed values (Welling et al., 2017). The degree to which this limits this study is uncertain, as contemporary validation studies of dB / dt values do not segregate skill as a function of activity type. Further validation is needed to understand model uncertainty associated with sudden impulses (Welling et al., 2018) and to understand how this uncertainty scales with impulse magnitude. The choice of F10.7 is critical as it sets the EUV conductance on the day side magnetosphere. For this simulation, the choice of 255 sfu was made to reflect values of contemporary extreme storms, but higher values are possible and even likely with such an extreme ICME. To provide some bounds for the impact of day side conductance, we can compare empirical estimates from Moen and Brekke (1993) at a solar zenith angle of 45° (corresponding to the position of strongest dB / dt values in this work) for F10.7 of 255 and 610 sfu. A doubling of F10.7 increases the Hall and Pedersen EUV conductance values by approximately 30%, intensifying day side currents somewhat and increasing the total dB / dt response. Finally, the issue of an electrostatic ionosphere must be raised. With high time frequency dynamics, the assumption of electrostatic coupling is likely to break down and inductive effects may become important. While this issue has been raised by others and alternative coupling strategies prototyped (Lotko, 2004; Sokolov et al., 2013; Song et al., 2009; Yoshikawa et al., 2010; Tu et al., 2011; Vanhamäki, 2011), none have been robustly validated for routine use with global MHD models. Considering these shortcomings, the ground magnetic perturbation estimates from these simulations should be considered a lower limit for a real-world event.

Further work is required to fully tie ICME arrival to consequences for the power grid. dB / dt, while clearly related to Geomagnetically Induced Currents (GICs), is not the value of most direct interest. Geoelectric field must be calculated using the ground impedance. This means accounting for the effects of an inhomogeneous conducting crust, lithosphere, and ocean. Incorporating this effect will be a priority of future studies. The estimates here yield an initial idea of the magnitudes of the geoelectric fields, but more work is required to improve upon these estimates, such as accounting for the three-dimensional structure of ground conductivity. It is also important to note that it is not just the geoelectric field amplitude, but also spectral content that affects the power grid. These must be further examined to understand the precise impact such an event would have on power transmission.

Despite these shortcomings, this work stands as an important indicator of the activity possible during the first moments after arrival of a "perfect" ICME at Earth. The magnitude of dB / dt, compression and erosion of the day side magnetopause, and short time scales for the onset of activity make such an event uniquely threatening to ground-based infrastructure. The penetration of activity to mid latitudes early in the event will affect regions not prepared for such strong geomagnetic activity, raising the vulnerability of power grids

in populated areas. Further exploring and preparing for such extreme activity is important to mitigate space weather related catastrophes.

Data Availability Statement

Model result data and input files are available via https://doi.org/10.5281/zenodo.3620786. The Space Weather Modeling Framework is maintained by the University of Michigan Center for Space Environment Modeling and can be obtained at http://csem.engin.umich.edu/tools/swmf. Analysis used the SWMF tools in the SpacePy package (Burrell et al., 2018; Morley et al., 2010). SpacePy is available at https://github.com/spacepy/spacepy.

Acknowledgments
The authors would like to thank Dr. Michael Wiltberger for providing his expertise to this project. The authors thank A. Kelbert and K. A. Lewis for reading a draft manuscript. This work was funded by the Laboratory Directed Research and Development (LDRD) program Grant 20170047DR and the National Science Foundation Award ICER-1663770. The authors would like to acknowledge high-performance computing support from Cheyenne (https://doi.org/10.5065/D6RX99HX, allocation UUSL0016) provided by NCAR's Computational and Information Systems Laboratory, sponsored by the National Science Foundation. Portions of this work by Dr Morley were performed under the auspices of the US Department of Energy. Dr Morley acknowledges additional support from Los Alamos National Laboratory's Center for Earth and Space Science through the Rapid Response program.

References

Allen, J., Sauer, H., Frank, L., & Reiff, P. (1989). Effects of the March 1989 solar activity. *Eos, Transactions American Geophysical Union*, *70*(46), 1479.https://doi.org/10.1029/89EO00409

Anderson, B. J., Korth, H., Welling, D. T., Merkin, V. G., Wiltberger, M. J., Raeder, J., et al. (2017). Comparison of predictive estimates of high-latitude electrodynamics with observations of global-scale Birkeland currents. *Space Weather*, *15*(2), 352–373. https://doi.org/10.1002/2016SW001529

Araki, T. (1977). Global structure of geomagnetic sudden commencements. *Planetary and Space Science*, *25*(4), 373–384. https://doi.org/10.1016/0032-0633(77)90053-8

Araki, T. (2014). Historically largest geomagnetic sudden commencement (SC) since 1868. *Earth Planets and Space*, *66*, 1–6. https://doi.org/10.1186/s40623-014-0164-0

Araki, T., Fujitani, S., Emoto, M., Yumoto, K., Shiokawa, K., Ichinose, T., & Liu, C. F. (1997). Anomalous sudden commencement on March 24, 1991. *Journal of Geophysical Research*, *102*(A7), 14075–14086. https://doi.org/10.1029/96JA03637

Baker, D. N., Li, X., Pulkkinen, A., Ngwira, C. M., Mays, M. L., Galvin, A. B., & Simunac, K. D. C. (2013). A major solar eruptive event in July 2012: Defining extreme space weather scenarios. *Space Weather*, *11*(10), 585–591. https://doi.org/10.1002/swe.20097

Bolduc, L. (2002). GIC observations and studies in the Hydro-Québec power system. *Journal of Atmospheric and Solar-Terrestrial Physics*, *64*(16), 1793–1802. https://doi.org/10.1016/S1364-6826(02)00128-1

Boteler, D. H. (2015). The evolution of Québec Earth models used to model geomagnetically induced currents. *IEEE Transactions on Power Delivery*, *30*(5), 2171–2178. https://doi.org/10.1109/TPWRD.2014.2379260

Boteler, D. H. (2019). A 21st century view of the March 1989 magnetic storm. *Space Weather*, *17*(10), 1427–1441. https://doi.org/10.1029/2019SW002278

Burrell, A. G., Halford, A., Klenzing, J., Stoneback, R. A., Morley, S. K., Annex, A. M., et al. (2018). Snakes on a spaceship—An overview of Python in Heliophysics. *Journal of Geophysical Research: Space Physics*, *123*, 10384–10402. https://doi.org/10.1029/2018JA025877

Cannon, P., Angling, M., Barclay, L., Curry, C., Dyer, C., Edwards, R., et al. (2013). *Extreme space weather: Impacts on engineered systems and infrastructure*. Royal Academy of Engineering.

De Zeeuw, D., Gombosi, T., Groth, C., Powell, K., & Stout, Q. (2000). An adaptive MHD method for global space weather simulations. *IEEE Transactions on Plasma Science*, *28*(6), 1956–1965. http://doi.org/10.1109/27.902224

De Zeeuw, D. L., Sazykin, S., Wolf, R. A., Gombosi, T. I., Ridley, A. J., & Tóth, G. (2004). Coupling of a global MHD code and an inner magnetospheric model: Initial results. *Journal of Geophysical Research*, *109*, A12219. https://doi.org/10.1029/2003JA010366

Eastwood, J. P., Biffis, E., Hapgood, M. A., Green, L., Bisi, M. M., Bentley, R. D., & Burnett, C. (2017). The economic impact of space weather. Where Do We Stand?*Risk Analysis*, *37*(2), 206–218. http://doi.wiley.com/10.1111/risa.12765

Glocer, A. (2016). Coupling ionospheric outflow into magnetospheric models. In *AGU monograph series* (pp. 195–203). Hoboken, NJ: John Wiley & Sons, Inc. https://doi.org/10.1002/9781119066880.ch15

Gonzalez, W. D., de Gonzalez, A. L. C., Dal Lago, A., Tsurutani, B. T., Arballo, J. K., Lakhina, G. K., et al. (1998). Magnetic cloud field intensities and solar wind velocities. *Geophysical Research Letters*, *25*(7), 963–966. https://doi.org/10.1029/98GL00703

Gonzalez, W. D., Echer, E., Tsurutani, B. T., De Gonzalez, A. L., & Dal Lago, A. (2011). Interplanetary origin of intense, superintense and extreme geomagnetic storms. In *Space science reviews* (Vol. 158, pp. 69–89). Netherlands: Springer. https://doi.org/10.1007/s11214-010-9715-2

Groth, C. P. T., De Zeeuw, D. L., Gombosi, T. I., & Powell, K. G. (2000). Global three-dimensional MHD simulation of a space weather event: CME formation, interplanetary propagation, and interaction with the magnetosphere. *Journal of Geophysical Research*, *105*(A11), 25053. https://doi.org/10.1029/2000JA900093

Guo, X. C., Hu, Y. Q., & Wang, C. (2005). Earth's magnetosphere impinged by interplanetary shocks of different orientations. *Chinese Physics Letters*, *22*(12), 3221–3224. https://doi.org/10.1088/0256-307X/22/12/067

Haiducek, J. D., Welling, D. T., Ganushkina, N. Y., Morley, S. K., & Ozturk, D. S. (2017). SWMF global magnetosphere simulations of January 2005: Geomagnetic indices and cross-polar cap potential. *Space Weather*, *15*(12), 1567–1587. https://doi.org/10.1002/2017SW001695

Haiducek, J. D., Welling, D. T., Morley, S. K., Ganushkina, N. Y., & Chu, X. (2020). Using multiple signatures to improve accuracy of substorm Identification. *Journal of Geophysical Research: Space Physics*, *125*, e2019JA027559. https://doi.org/10.1029/2019JA027559

Harel, M., Wolf, R. A., Reiff, P. H., Spiro, R. W., Burke, W. J., Rich, F. J., & Smiddy, M. (1981). Quantitative simulation of a magnetospheric substorm. 1: Model logic and overview. *Journal of Geophysical Research*, *86*(A4), 2217. https://doi.org/10.1029/JA086iA04p02217

Ilie, R., Liemohn, M. W., & Ridley, A. (2010). The effect of smoothed solar wind inputs on global modeling results. *Journal of Geophysical Research*, *115*, A01213. https://doi.org/10.1029/2009JA014443

Jolliffe, I. T., & Stephenson, D. B. (2012). *Forecast verification: A practitioner's guide in atmospheric science*. John Wiley & Sons. Retrieved from https://books.google.com/books?hl=en&lr=&id=DCxsKQeaBH8C&pgis=1

Joselyn, J. A., & Tsurutani, B. T. (1990). Geomagnetic sudden impulses and storm sudden commencements: A note on terminology. *Eos, Transactions American Geophysical Union*, *71*(47), 1808–1809. http://doi.org/10.1029/90EO00350

Kappenman, J. G. (2005). An overview of the impulsive geomagnetic field disturbances and power grid impacts associated with the violent Sun-Earth connection events of 29–31 October 2003 and a comparative evaluation with other contemporary storms. *Space Weather*, *3*(8), S08C01. http://doi.org/10.1029/2004SW000128

Kataoka, R., Fukunishi, H., Fujita, S., Tanaka, T., & Itonaga, M. (2004). Transient response of the Earth's magnetosphere to a localized density pulse in the solar wind: Simulation of traveling convection vortices. *Journal of Geophysical Research*, *109*, A03204. https://doi.org/10.1029/2003JA010287

Korth, H., Rastätter, L., Anderson, B. J., & Ridley, A. J. (2011). Comparison of the observed dependence of large-scale Birkeland currents on solar wind parameters with that obtained from global simulations. *Annales Geophysicae*, *29*(10), 1809–1826. https://doi.org/10.5194/angeo-29-1809-2011

Lakhina, G. S., Alex, S., Tsurutani, B. T., & Gonzalez, W. D. (2012). Supermagnetic storms: Hazard to society. Geophysical Monograph Series (Vol. 196, pp. 267–278). Washington, DC:American Geophysical Union. https://doi.org/10.1029/2011GM001073

Li, X., Temerin, M., Tsurutani, B., & Alex, S. (2006). Modeling of 1–2 September 1859 super magnetic storm. *Advances in Space Research*, *38*(2), 273–279. http://doi.org/10.1016/j.asr.2005.06.070

Lotko, W. (2004). Inductive magnetosphere–ionosphere coupling. *Journal of Atmospheric and Solar-Terrestrial Physics*, *66*(15–16), 1443–1456. https://doi.org/10.1016/J.JASTP.2004.03.027

Love, J. J., Bedrosian, P. A., Kelbert, A., & Lucas, G. M. (2019). Empirical estimation of natural geoelectric hazards(pp. 93–105). Washington, DC:American Geophysical Union. https://doi.org/10.1002/9781119434412.ch6

Love, J. J., Hayakawa, H., & Cliver, E. W. (2019a). Intensity and impact of the New York railroad Superstorm of May 1921. *Space Weather*, *17*(8), 1281–1292. https://doi.org/10.1029/2019sw002250

Love, J. J., Hayakawa, H., & Cliver, E. W. (2019b). On the intensity of the magnetic Superstorm of September 1909. *Space Weather*, *17*(1), 37–45. https://doi.org/10.1029/2018SW002079

Love, J. J., Lucas, G. M., Bedrosian, P. A., & Kelbert, A. (2019). Extreme-value geoelectric amplitude and Polarization across the Northeast United States. *Space Weather*, *17*(3), 379–395. https://doi.org/10.1029/2018SW002068

Manchester, W., Ridley, A., Gombosi, T., & DeZeeuw, D. (2006). Modeling the Sun-to-Earth propagation of a very fast CME. *Advances in Space Research*, *38*(2), 253–262. https://doi.org/10.1016/j.asr.2005.09.044

Moen, J., & Brekke, A. (1993). The solar flux influence on quiet time conductances in the auroral ionosphere. *Geophysical Research Letters*, *20*(10), 971–974. https://doi.org/10.1029/92GL02109

Morley, S. K. S., Welling, D. D. T., Koller, J., Larsen, B. A., Henderson, M. G., & Niehof, J. (2010). *SpacePy—A python-based library of tools for the space sciences. Paper presented at the Proceeding of the 9th Python in Science Conference*. (pp. 39–45). Austin, TX. Retrieved from https://projects.scipy.org/proceedings/scipy2010/pdfs/morley.pdfhttp://conference.scipy.org/proceedings/scipy2010/pdfs/morley.pdf

Mukhopadhyay, A., Welling, D. T., Liemohn, M. W., Ridley, A. J., Chakraborty, S., & Anderson, B. J. (2020). *Conductance model for extreme events: Impact of auroral conductance on space weather forecasts*, 18, 11, 1–36. Space Weather. https://doi.org/10.1029/2020SW002551

National Research Committee on the Societal and Economic Impacts of Severe Space Weather Events (2008). *Workshop report (Tech. Rep.)*. Washington, DC:The National Academies Press. https://doi.org/10.17226/12507

National Science and Technology Council. (2015). National space weather action plan (Tech. Rep.). Retrieved from https://www.whitehouse.gov/sites/default/files/microsites/ostp/final_nationalspaceweatheractionplan_20151028.pdf

Ngwira, C. M., Pulkkinen, A., Kuznetsova, M. M., & Glocer, A. (2014). Modeling extreme "Carrington-type" space weather events using three-dimensional global MHD simulations. *Journal of Geophysical Research: Space Physics*, *119*, 4456–4474. https://doi.org/10.1002/2013JA019661

Ngwira, C. M., Pulkkinen, A., Leila Mays, M., Kuznetsova, M. M., Galvin, A. B., Simunac, K., et al. (2013). Simulation of the 23 July 2012 extreme space weather event: What if this extremely rare CME was Earth directed?. *Space Weather*, *11*(12), 671–679. https://doi.org/10.1002/2013SW000990

Oliveira, D. M., Arel, D., Raeder, J., Zesta, E., Ngwira, C. M., Carter, B. A., et al. (2018). Geomagnetically induced currents caused by interplanetary shocks with different impact angles and speeds. *Space Weather*, *16*(6), 636–647. https://doi.org/10.1029/2018SW001880

Oliveira, D. M., & Raeder, J. (2014). Impact angle control of interplanetary shock geoeffectiveness. *Journal of Geophysical Research: Space Physics*, *119*, 8188–8201. https://doi.org/10.1002/2014JA020275

Oliveira, D. M., & Raeder, J. (2015). Impact angle control of interplanetary shock geoeffectiveness: A statistical study. *Journal of Geophysical Research: Space Physics*, *120*, 4313–4323. https://doi.org/10.1002/2015JA021147

Palacky, G. J. (1988). Resistivity characteristics of geologic targets. In *Electromagnetic methods in applied geophysics* (pp. 52–129). Society of Exploration Geophysicists. https://doi.org/10.1190/1.9781560802631.ch3

Pirjola, R. (1985). Electromagnetic induction in the Earth by a line current harmonic in time and space. *Geophysica*, *21*(2), 127–143.

Pirjola, R. (2005). Effects of space weather on high-latitude ground systems. *Advances in Space Research*, *36*(12), 2231–2240. https://doi.org/10.1016/j.asr.2003.04.074

PirjolaR. (2002). Review on the calculation of surface electric and magnetic fields and of geomagnetically induced currents in ground-based technological systems. *Surveys in Geophysics*, *23*(1), 71–90. https://doi.org/10.1023/A:1014816009303

Powell, K., Roe, P., & Linde, T. (1999). A solution-adaptive upwind scheme for ideal magnetohydrodynamics. *Journal of Computational Physics*, *154*(2), 284–309. https://doi.org/10.1006/jcph.1999.6299

Pulkkinen, A., Bernabeu, E., Eichner, J., Beggan, C., & Thomson, A. W. (2012). Generation of 100-year geomagnetically induced current scenarios. *Space Weather*, *10*, S04003. https://doi.org/10.1029/2011SW000750

Pulkkinen, A., Rastätter, L., Kuznetsova, M., Singer, H., Balch, C., Weimer, D., & Weigel, R. (2013). Community-wide validation of geospace model ground magnetic field perturbation predictions to support model transition to operations. *Space Weather*, *11*(6), 369–385. https://doi.org/10.1002/swe.20056

Rastätter, L., Kuznetsova, M. M., Glocer, A., Welling, D., Meng, X., Raeder, J., & Gannon, J. (2013). Geospace environment modeling 2008–2009 challenge: D st index. *Space Weather*, *11*(4), 187–205. https://doi.org/10.1002/swe.20036

Rastätter, L., Kuznetsova, M. M., Vapirev, A., Ridley, A., Wiltberger, M., Pulkkinen, A., et al. (2011). Geospace environment modeling 2008–2009 challenge: Geosynchronous magnetic field. *Space Weather*, *9*(4), S04005. Retrieved from https://doi.org/10.1029/2010SW000617

Ridley, A. J., De Zeeuw, D. L., Gombosi, T. I., & Powell, K. G. (2001). Using steady state MHD results to predict the global state of the magnetosphere-ionosphere system. *Journal of Geophysical Research*, *106*(A12), 30067. https://doi.org/10.1029/2000JA002233

Ridley, A., De Zeeuw, D., Manchester, W., & Hansen, K. (2006). The magnetospheric and ionospheric response to a very strong interplanetary shock and coronal mass ejection. *Advances in Space Research*, *38*(2), 263–272. https://doi.org/10.1016/j.asr.2006.06.010

Ridley, A. J., Hansen, K. C., Toth, G., DeZeeuw, D. L., Gombosi, T., & Powell, K. G. (2002). University of Michigan MHD results of the geospace global Circulation model metrics challenge. *Journal of Geophysical Research*, *107*(A10), 1290. https://doi.org/10.1029/2001JA000253

Sazykin, S., & Stanislav (2000). *Theoretical studies of penetration of magnetospheric electric fields to the ionosphere* (PhD thesis) (Source DAI-B 61/12, pp. 278). Utah State University.

Schrijver, C. J. (2015). Socio-economic hazards and impacts of space weather: The important range between mild and extreme. *Space Weather,13*(9), 524–528. https://doi.org/10.1002/2015SW001252

Simpson, J. J., & Taflove, A. (2005). Electrokinetic effect of the Loma Prieta earthquake calculated by an entire-Earth FDTD solution of Maxwell's equations. *Geophysical Research Letters*, *32*, L09302. https://doi.org/10.1029/2005GL022601

Slinker, S. P., Fedder, J. A., Emery, B. A., Baker, K. B., Lummerzheim, D., Lyon, J. G., & Rich, F. J. (1999). Comparison of global MHD simulations with AMIE simulations for the events of May 19–20, 1996. *Journal of Geophysical Research*, *104*(A12), 28379–28395. https://doi.org/10.1029/1999JA900403

Sokolov, I. V., Gombosi, T. I., & Ridley, A. J. (2013). Non-potential electric field model of magnetosphere-ionosphere coupling. In*Inner magnetosphere interactions: New perspectives from imaging* (Vol. 159, pp. 141–152). Washington, DC:American Geophysical Union. https://doi.org/10.1029/159GM10

Song, P., DeZeeuw, D. L., Gombosi, T. I., Groth, C. P. T., & Powell, K. G. (1999). A numerical study of solar wind–magnetosphere interaction for northward interplanetary magnetic field. *Journal of Geophysical Research*, *104*(A12) 28361. Retrieved from https://10.1029/1999JA900378

Song, P., Vasyliūnas, V. M., & Zhou, X.-Z. (2009). Magnetosphere-ionosphere/thermosphere coupling: Self-consistent solutions for a one-dimensional stratified ionosphere in three-fluid theory. *Journal of Geophysical Research*, *114*, A08213. https://doi.org/10.1029/2008JA013629

Toffoletto, F., Sazykin, S., Spiro, R., & Wolf, R. (2003). Inner magnetospheric modeling with the Rice convection model. *Space Science Reviews*, *107*,175–196. https://doi.org/10.1023/A:1025532008047

Tóth, G. (2000). The div B=0 Constraint in shock-capturing magnetohydrodynamics codes. *Journal of Computational Physics*, *161*(2), 605–652. https://doi.org/10.1006/jcph.2000.6519

Tóth, G., Sokolov, I. V., Gombosi, T. I., Chesney, D. R., Clauer, C. R., De Zeeuw, D. L., et al. (2005). Space weather modeling framework: A new tool for the space science community. *Journal of Geophysical Research*, *110*, A12226. https://doi.org/10.1029/2005JA011126

Tóth, G., van der Holst, B., Sokolov, I. V., De Zeeuw, D. L., Gombosi, T. I., Fang, F., et al. (2012). Adaptive numerical algorithms in space weather modeling. *Journal of Computational Physics*, *231*(3), 870–903. https://doi.org/10.1016/j.jcp.2011.02.006

Tsurutani, B. T. (2003). The extreme magnetic storm of 1–2 September 1859. *Journal of Geophysical Research*, *108*(A7), 1268. https://doi.org/10.1029/2002JA009504

Tsurutani, B. T., & Lakhina, G. S. (2014). An extreme coronal mass ejection and consequences for the magnetosphere and Earth. *Geophysical Research Letters*, *41*, 287–292. https://doi.org/10.1002/2013GL058825

Tu, J., Song, P., & Vasylinas, V. M. (2011). Ionosphere/thermosphere heating determined from dynamic magnetosphere-ionosphere/thermosphere coupling.*Journal of Geophysical Research*, *116*, A09311. https://doi.org/10.1029/2011JA016620

Vanhamäki, H. (2011). Inductive ionospheric solver for magnetospheric MHD simulations. *Annales Geophysicae*, *29*(1), 97–108. https://doi.org/10.5194/angeo-29-97-2011

Wait, J. (1982). *Geo-electromagnetism*. New York, NY: Academic Press.

Wang, C., Li, C. X., Huang, Z. H., & Richardson, J. D. (2006). Effect of interplanetary shock strengths and orientations on storm sudden commencement rise times. *Geophysical Research Letters*, *33*, L14104. https://doi.org/10.1029/2006GL025966

Welling, D. (2019). Magnetohydrodynamic models of B and their use in GIC estimates. In J. L.Gannon, A.Swidinsky, & Z.Xu, (Eds.). *Geomagnetically induced currents from the sun to the power grid* (Geophysica ed., pp. 43–65). Washington, DC: American Geophysical Union (AGU). Retrieved from https://doi.org/10.1002/9781119434412.ch3

Welling, D. T., Anderson, B. J., Crowley, G., Pulkkinen, A. A., & Rastätter, L. (2017). Exploring predictive performance: A reanalysis of the geospace model transition challenge. *Space Weather*, *15*(1), 192–203. https://doi.org/10.1002/2016SW001505

Welling, D. T., Jordanova, V. K., Glocer, A., Toth, G., Liemohn, M. W., & Weimer, D. R. (2015). The two-way relationship between ionospheric outflow and the ring current. *Journal of Geophysical Research: Space Physics*, *120*, 4338–4353. https://doi.org/10.1002/2015JA021231

Welling, D. T., Ngwira, C. M., Opgenoorth, H. J., Haiducek, J. D., Savani, N. P., & Morley, et al. (2018). Recommendations for next-generation ground magnetic perturbation validation. *Space Weather*, *16*(12), 4338–4353. https://doi.org/10.1029/2018SW002064

Welling, D. T., & Ridley, A. J. (2010). Exploring sources of magnetospheric plasma using multispecies MHD. *Journal of Geophysical Research*, *115*, A04201. https://doi.org/10.1029/2009JA014596

Welling, D. T., & Zaharia, S. G. (2012). Ionospheric outflow and cross polar cap potential: What is the role of magnetospheric inflation?. *Geophysical Research Letters*, *39*, L23101. https://doi.org/10.1029/2012GL054228

Woodroffe, J. R., Morley, S. K., Jordanova, V. K., Henderson, M. G., Cowee, M. M., & Gjerloev, J. G. (2016). The latitudinal variation of geoelectromagnetic disturbances during large (Dst -100 nT) geomagnetic storms. *Space Weather*, *14*(9), 668–681. https://doi.org/10.1002/2016SW001376

Yoshikawa, A., Nakata, H., Nakamizo, A., Uozumi, T., Itonaga, M., Fujita, S., et al. (2010). Alfvenic-coupling algorithm for global and dynamical magnetosphere-ionosphere coupled system. *Journal of Geophysical Research*, *115*, A04211. https://doi.org/10.1029/2009JA014924

Yu, Y., & Ridley, A. J. (2008). Validation of the space weather modeling framework using ground-based magnetometers. *Space Weather*, *6*(5), S05002. https://doi.org/10.1029/2007SW000345

Yu, Y., & Ridley, A. J. (2009a). The response of the magnetosphere-ionosphere system to a sudden dynamic pressure enhancement under southward IMF conditions. *Annales Geophysicae*, *27*(12), 4391–4407.https://doi.org/10.5194/angeo-27-4391-2009

Yu, Y., & Ridley, A. J. (2009b). Response of the magnetosphere-ionosphere system to a sudden southward turning of interplanetary magnetic field. *Journal of Geophysical Research*, *114*, A03216. https://doi.org/10.1029/2008JA013292

Zhang, J., Liemohn, M. W., De Zeeuw, D. L., Borovsky, J. E., Ridley, A. J., Toth, G., et al. (2007). Understanding storm-time ring current development through data-model comparisons of a moderate storm. *Journal of Geophysical Research*, *112*, A04208. https://doi.org/10.1029/2006JA011846